Cellular Uptake of Nanoparticles by Membrane Penetration: A Study Combining Confocal Microscopy with FTIR Spectroelectrochemistry

Tiantian Wang,[†,‡] Jing Bai,[†] Xiue Jiang,[†,*] and G. Ulrich Nienhaus[§,⊥]

[†]State Key Laboratory of Electroanalytical Chemistry, Changchun Institute of Applied Chemistry, Chinese Academy of Sciences, Changchun 130022, China, [‡]Graduate School of Chinese Academy of Sciences, Beijing 100049, China, [§]Institute of Applied Physics and Center for Functional Nanostructures (CFN), Karlsruhe Institute of Technology (KIT), Wolfgang-Gaede-Strasse 1, 76131 Karlsruhe, Germany, and [⊥]Department of Physics, University of Illinois at Urbana—Champaign, Urbana, Illinois 61801, United States

ABSTRACT

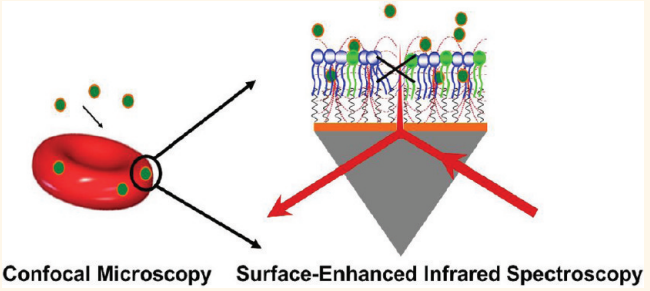

It is well-known that nanomaterials are capable of entering living cells, often by utilizing the cells' endocytic mechanisms. Passive penetration of the lipid bilayer may, however, occur as an alternative process. Here we have focused on the passive transport of small nanoparticles across the plasma membranes of red blood cells, which are incapable of endocytosis. By using fluorescence microscopy, we have observed that zwitterionic quantum dots penetrate through the cell membranes so that they can be found inside the cells. The penetration-induced structural changes of the lipid bilayer were explored by surface-enhanced infrared absorption spectroscopy and electrochemistry studies of model membranes prepared on solid supports with lipid compositions identical to those of red blood cell membranes. A detailed analysis of the infrared spectra revealed a markedly enhanced flexibility of the lipid bilayers in the presence of nanoparticles. The electrochemistry data showed that the overall membrane structure remained intact; however, no persistent holes were formed in the bilayers.

KEYWORDS: zwitterionic quantum dots · membrane penetration mechanism · pore formation · FTIR spectroelectrochemistry · confocal microscopy

In recent years, the use of engineered nanoparticles in research and technology has been rapidly expanding; nanoparticles have become part of our daily life in medical, cosmetic, or food products.[1] For example, in biomedicine, nanomaterials are widely employed as diagnostic imaging tools,[2] drug delivery carriers,[3] and gene therapy agents.[4] This development inevitably increases the chance of human exposure to nanoparticles. Owing to their small size, they can potentially penetrate physiological barriers and invade all parts of the body, tissues, cells, and even subcellular compartments. Concerns have arisen that nanoparticle exposure may lead to adverse health effects.[5] Therefore, a profound understanding of the interactions of nanoparticles with living cells and organisms is indispensable for their safe and beneficial use while avoiding possible biological hazards.

Upon nanoparticle exposure, cells incorporate nanoparticles across the fluid plasma membrane, either by endocytosis (*i.e.*, actively by using the cellular uptake machinery) or by passive penetration.[6−12] During endocytosis, nanoparticles are enclosed by endocytic vesicles and are thus not directly transferred into the cytosol. By contrast, nanoparticles internalized by membrane penetration enter the cytosol directly, which can be preferable for targeted drug delivery agents. Often, cytotoxicity is observed upon nanoparticle exposure, which may arise—at least in part—from nonspecific adhesion of nanoparticles to the cell membranes and the resulting effects on membrane morphology or permeability. Therefore, studying the interaction of nanoparticles with cell membranes is a first important step toward understanding the concomitant biological responses.

The ability of nanoparticles to adhere to and penetrate cell membranes is governed by their physical properties including size, surface composition, and surface charge.[11,13−17] Nanomaterials with very small dimensions and positive charge have been observed to

* Address correspondence to jiangxiue@ciac.jl.cn.

Received for review October 10, 2011 and accepted January 1, 2012.

Published online January 17, 2012
10.1021/nn203892h

pass through cell membranes by forming membrane holes, generating noticeable cytotoxic effects in the process.[18−21] Even particles larger than 500 nm in diameter can penetrate cell membranes by inducing strong local membrane deformations.[22] However, membrane disruptions can be reduced or even completely avoided by modulating the surface charge density or surface structure.[11,23] Therefore, it appears feasible that synthetic materials with optimally engineered surface properties may pass through membranes without disrupting the cell membrane.

Colloidal semiconductor core/shell quantum dots (QDs) hold great promise for applications in biotechnology and biomedicine due to their small size (diameter 1−5 nm), brightness, and photostability.[24−27] Recently, we have shown that CdSe/ZnS core/shell QDs coated with the zwitterionic thiol ligand D-penicillamine (DPA-QDs) feature much improved colloidal stability in physiological media and can be effectively internalized into living cells, predominantly *via* clathrin-mediated endocytosis.[28,29] The small DPA ligand adds minimally to the overall size of the nanoparticle. DPA-QDs effectively resemble small globular proteins with regard to size, near-neutral charge, and surface functional groups (amine and carboxylic acid groups). Even after inhibition of all actin-dependent uptake pathways, we still observed DPA-QD internalization by human cells in culture, which suggests that they may be capable of penetrating the plasma membrane. These results motivated us to investigate DPA-QD uptake by red blood cells (RBCs), highly specialized cells lacking a cell nucleus, most organelles, and the endocytic machinery.[30] Therefore, they have been used as a model system for studying the passive movement of nanoparticles across the plasma membrane.[31−33] The presence of such a passive mechanism has been inferred from observing very few polystyrene and titanium dioxide nanoparticles inside RBCs upon exposure to these nanoparticles.[32,33]

In this work, we have studied the penetration of DPA-QDs into RBCs by fluorescence imaging. In addition, we have investigated the interaction between DPA-QDs and model membranes having lipid compositions identical to those of RBC membranes. These membranes were prepared on solid supports and studied by electrochemistry and surface-enhanced infrared absorption spectroscopy (SEIRAS) to gain insight into the molecular processes. Importantly, we were able to show that penetration of the lipid membrane by DPA-QDs occurs without formation of holes in the bilayer.

RESULTS AND DISCUSSION

Confocal Microscopy of RBCs Exposed to DPA-QDs. We incubated RBCs with phosphate buffered saline (PBS) solutions containing 10 nM DPA-QDs of 4 nm radius and imaged them by using spinning disk confocal

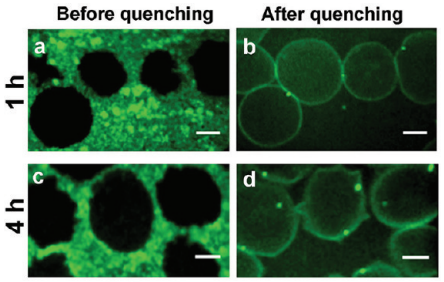

Figure 1. Confocal fluorescence images of DPA-QDs interacting with RBCs. RBCs were incubated with 10 nM DPA-QDs for (a,b) 1 h and (c,d) 4 h, washed, and incubated with QSY 9 for 10 min at a concentration of 5 μg/mL to quench the fluorescence of DPA-QDs adsorbed onto the chamber surface and the cells. Images before and after quencher application are shown in panels a,c and b,d, respectively. Scale bar: 5 μm.

microscopy. The physicochemical properties of the DPA-QDs have been characterized thoroughly in previous work.[29] In a study addressing endo- and exocytosis of DPA-QDs by live HeLa cells, these nanoparticles were observed to accumulate on the cell membrane within 1 min after incubation and were subsequently internalized and transported to the perinuclear region over the ensuing hour.[29] By contrast, membrane accumulation and internalization of DPA-QDs were not observed with RBCs, even after 4 h of incubation (Figure 1a,c). The DPA-QDs rather adhered to the surface of the incubation chamber where they produced a strong fluorescence background, so that the attached cells are seen as dark circles in the images. If only a small number of QDs had been internalized, the strong surface fluorescence would have precluded their unambiguous detection under these conditions.

To eliminate the strong fluorescence from surface-adsorbed DPA-QDs, cells were treated with QSY 9 after 1 or 4 h of incubation with 10 nM DPA-QDs (Figure 1b,d). QSY 9 is a nonfluorescent dye with a broad and intense absorption in the range of 500−650 nm that quenches the fluorescence of other dyes in close proximity by Förster resonance energy transfer. A similar approach had been employed by Hoeksira *et al.*[34] to discriminate between cell association and the actual internalization of nanoparticles. They exposed the cells to high concentrations of Trypan Blue to quench the extracellular fluorescence. Compared with the confocal images taken prior to QSY 9 application (Figure 1a,c), the strong fluorescence from the adsorbed DPA-QDs on the surface essentially disappeared after application of QSY 9 (Figure 1b,d). Notably, after QSY 9 quenching, the RBC membranes appear stained by DPA-QDs, and furthermore, a few fluorescent spots are clearly visible inside the cells after 1 h incubation (Figure 1b). Even more spots are found after 4 h incubation (Figure 1d). We can safely conclude from this experiment that the staining of the RBC membrane must arise from DPA-QDs that are not in contact

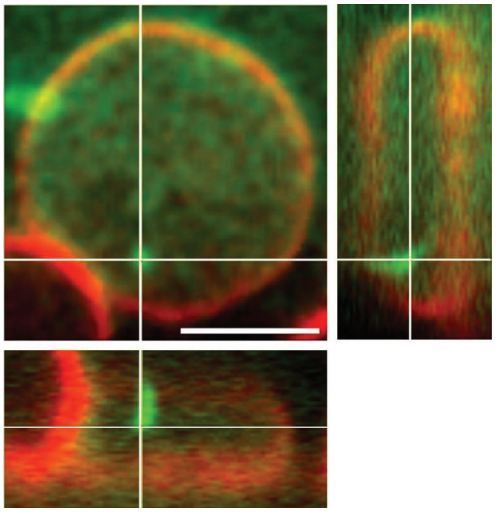

Figure 2. Three-dimensional reconstructions of confocal image stacks showing the internalization of DPA-QDs by RBCs. The data are represented as sections in the *x*−*y* plane (upper left), *x*−*z* plane (lower), and *y*−*z* plane (upper right). Scale bar: 5 μm.

with the extracellular medium. Apparently, DPA-QDs penetrate the RBC membrane and remain either within the bilayer or associate with the inner membrane surface. Moreover, the fluorescent spots inside the cells (Figure 1b,d), which are much brighter than individual DPA-QDs, reveal their ability to migrate and cluster inside the RBCs. Three-dimensional image stacks were also recorded (Figure 2). From the sections in the *x*−*z* and *y*−*z* planes, it is obvious that measurements in the *x*−*y* plane, taken at a *z*-position of about half the height of the cell, allow us to reliably assign the bright spots to intracellular regions.

Additionally, we studied the interactions between DPA-QDs and RBCs in an alternative way that entirely eliminates interference from surface fluorescence. To this end, RBCs were treated with 10 nM DPA-QDs in PBS solution for different times in a humidified incubator at 37 °C and 5% CO_2. Subsequently, the solution was centrifuged to separate free DPA-QDs from the RBCs, and the sedimented cells were transferred into a sample cell for imaging. In Figure 3, bright-field and fluorescence confocal images are overlaid for a control sample (without DPA-QD exposure) and for samples incubated with DPA-QDs for 1, 4, and 8 h. From these images, it is clearly evident that the cell membranes are stained by DPA-QDs, and the number of fluorescence spots, which are either close to the cell membranes or inside the cells, increases with the incubation time (Figure 3b−d). The internalization kinetics (Figure 3e) was obtained by calculating the integrated fluorescence intensity of the internal spots (red circles) and normalizing them to the cellular area in the observation plane. The internalized fraction increased with a half-life of 1.7 h. Upon DPA-QD exposure, the RBC surfaces still had a smooth appearance, similar to the

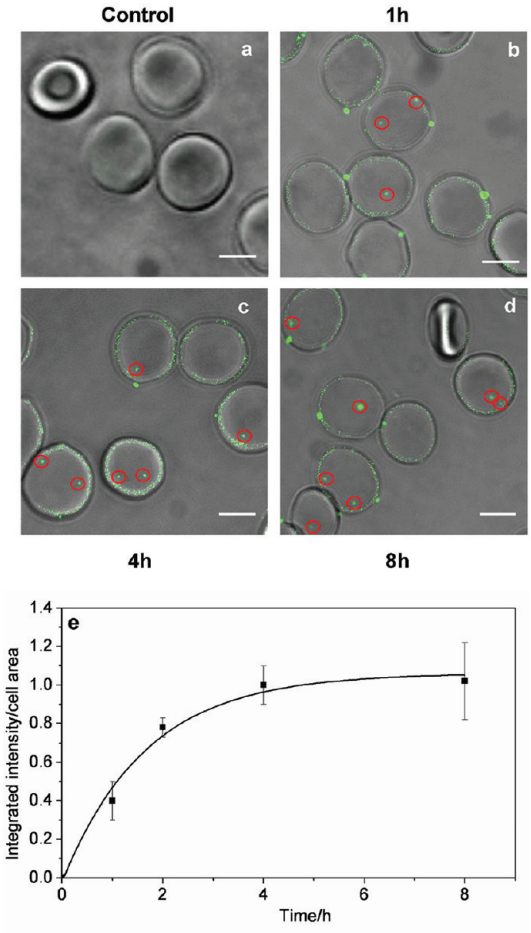

Figure 3. Confocal fluorescence and bright-field (overlay) images of DPA-QD internalization by RBCs. RBCs were incubated with (a) PBS as control, and 10 nM DPA-QDs for (b) 1 h, (c) 4 h, and (d) 8 h. Scale bar: 5 μm. (e) Integrated fluorescence intensity of intracellular bright spots normalized to the cellular area observed in the section, plotted as a function of time. For each time point, eight images from three different experiments were analyzed; error bars indicate standard deviations from the mean.

control RBCs, so the DPA-QDs did not induce a strong local membrane deformation, at least on a spatial scale that can be resolved by optical microscopy. Penetration of DPA-QDs into RBCs appears not to disturb the integrity of the membrane or even induce formation of pores, which should result in an aberrant morphology of the RBC membranes.[35]

To further test this proposition, we checked if DPA-QDs' internalization allowed the escape of a tracer dye from the cytosol.[11] RBCs were preincubated with calcein violet AM (Figure 4a), a cell-membrane-permeant dye that becomes impermeant after hydrolysis by intracellular esterases. Subsequently, cells were incubated with DPA-QDs for 6 h. As seen in Figure 4b and supported by the quantitative image analysis in Figure 4c, internalization of DPA-QDs did not cause any loss of cellular fluorescence from the dye. Entrance of DPA-QDs without causing any measurable leakage of

calcein violet AM suggests that the RBC membranes remain largely intact in the process.

Electrochemistry Study of the Interaction of DPA-QDs with a Planar Model Membrane. To further strengthen the evidence that DPA-QD penetration through RBC membranes did not induce holes, we studied the DPA-QD exposure to model membranes by electrochemistry, a label-free approach. To explore the effect of DPA-QDs interacting with the outer and inner lipid layer of RBC membranes, we produced, by vesicle fusion, planar lipid bilayers on a solid support having identical lipid compositions as the outer and inner leaflets of RBC plasma membranes. The outer lipid leaflet consists mainly of phosphatidylcholine (PC), sphingomyelin (SM), the inner one mainly of phosphatidylethanolamine (PE) and phosphatidylserine (PS), whereas cholesterol is evenly distributed.[36] In our study, we used egg PC, SM, and cholesterol to mimic the outer leaflet and dioleoyl phosphoethanolamine (DOPE), dioleoyl phosphatidylserine (DOPS), and cholesterol to mimic the inner lipid leaflet. Vesicles with the lipid content of the outer or inner lipid layer were fused on a solid support by the hydrophobic interaction between the vesicles and the hydrophobic surface of a self-assembled monolayer of 1-dodecanethiol (DT) preadsorbed on a gold electrode (Figure 5). Pore formation in a supported bilayer (*e.g.*, by DPA-QD penetration) can be inferred from monitoring the transport capability of an electroactive ionic species, $[Fe(CN)_6]^{3-}$, through the lipid bilayer before and after nanoparticle exposure. Each preparation step was confirmed by cyclic voltammetry (CV) and SEIRAS.

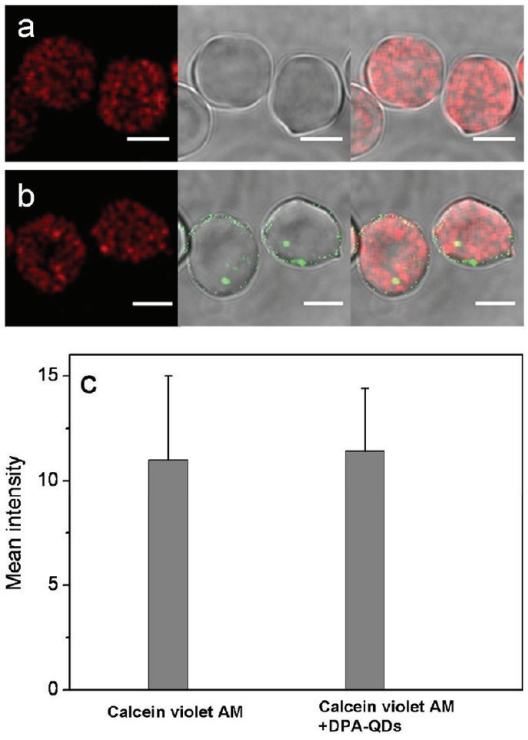

Figure 4. Fluorescence microscopy experiment examines if DPA-QD uptake by RBCs causes holes in the plasma membrane. RBCs were incubated with (a) calcein violet AM, and subsequently (b) with 10 nM DPA-QDs for 6 h. Scale bar: 5 μm. (c) Mean fluorescence intensities of calcein violet AM labeled cells, averaged over 70−90 cells from two different experiments.

Figure 6 shows the electrochemical behavior of the fresh Au electrode in 5 mM $[Fe(CN)_6]^{3-}$ solution with 0.1 M KCl (black). A quasi-reversible redox couple with a cathodic and an anodic peak at 0.17 and 0.26 V *versus* Ag/AgCl indicates a fast electron transfer. After incubation of the bare Au electrode with DT, the electrode was scanned in the same solution. Comparison of the black and red curves in Figure 6a,b reveals significantly decreased peak currents and an increased peak-to-peak separation (red) due to formation of a DT monolayer on the Au electrode slowing down the electron transfer kinetics of the probe. By adjusting the assembly time of the DT monolayer, we can fine-tune the density to yield a pervious, thin film and ensure initiation of spontaneous vesicle fusion. After vesicle fusion on the DT monolayer, the current peaks were completely eliminated, indicating a defect-free planar membrane blocking the electrode surface (Figure 6a,b, green). Upon treatment of the model membrane with DPA-QD solution for 1 and 8 h, the currents were further decreased for both systems (Figure 6a,b, blue and cyan). This experiment clearly indicates that the

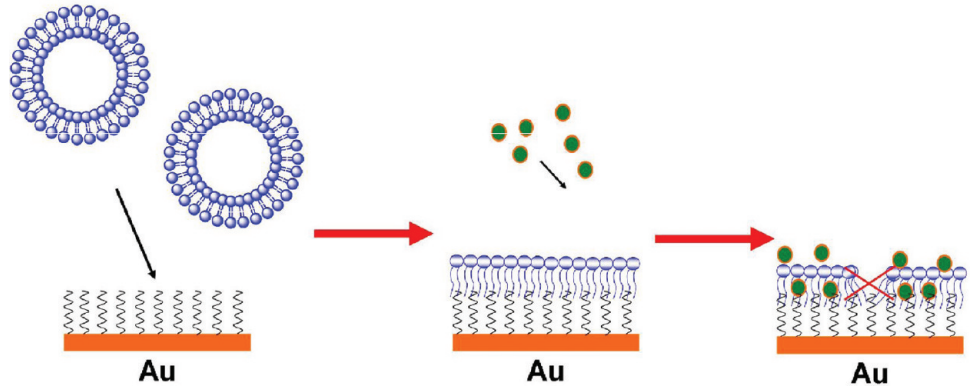

Figure 5. Schematic diagram illustrating the interaction of DPA-QDs with planar membranes, formed by hydrophobic interactions between vesicles and hydrophobic DT monolayers self-assembled on a gold electrode.

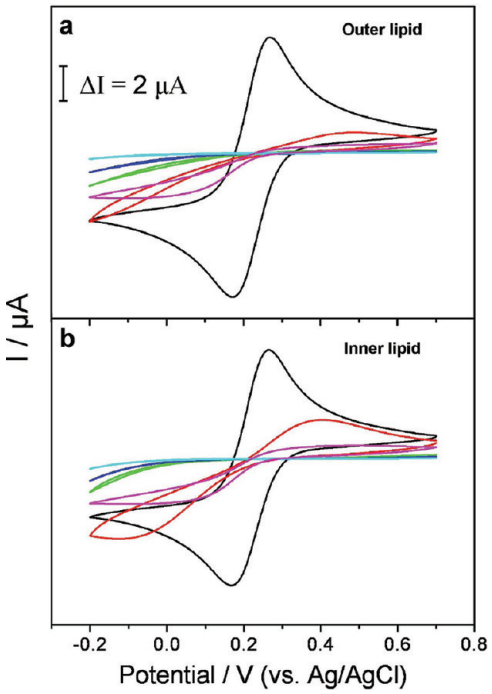

Figure 6. Electrochemistry study of DPA-QDs interacting with a planar lipid bilayer. The planar lipid bilayer was constituted by vesicle fusion composed of a mixture of (a) egg PC, SM, and cholesterol; (b) DOPE, DOPS, and cholesterol. Cyclic voltammograms of 5 mM $[Fe(CN)_6]^{3-}$ in a solution of 0.1 M KCl. Cyclic voltammograms carried out with (a,b) bare Au (black), DT/Au (red), and lipid/DT/Au (green) working electrodes. The cyclic voltammograms shown in blue and cyan were obtained with the lipid/DT/Au electrode after exposing the electrode to a 10 nM DPA-QD solution for 1 and 8 h, respectively. Afterward, the electrode was treated with 1% poly(ethyleneimine) solution for 1 h (magenta). The scan rate was 50 mV/s.

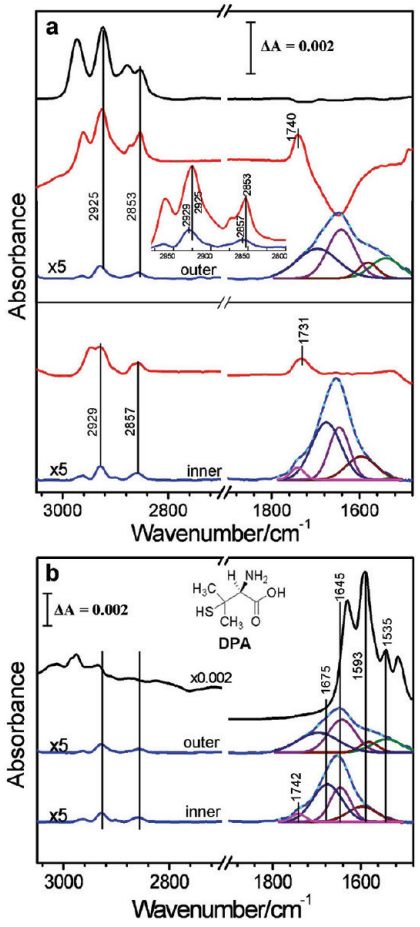

Figure 7. SEIRAS experiments to study the interaction of DPA-QDs with preformed planar membranes. (a) Spectra of a monolayer of DT adsorbed on the gold surface (black), vesicles containing the lipids of the outer (upper panel) and inner (lower panel) lipid leaflet of RBCs adsorbed on the DT-modified gold surface (red), and DPA-QDs adsorbed on the lipid/DT modified gold surface (blue), including Gaussian bands obtained by curve fitting (the individual bands are shown underneath the blue spectrum). (b) Spectra of DPA-QDs adsorbed on the lipid/DT modified gold surface (blue) are plotted together with the transmission spectrum of DPA in a KBr pellet (black).

presence of DPA-QDs did not generate pores in the outer and inner lipid layers of RBC membranes because this process would strongly change the CV response of the membrane-modified electrode (Figure 6a,b, magenta). After the planar membranes were incubated with 1% poly(ethyleneimine) (PEI) for 1 h, the redox current of $[Fe(CN)_6]^{3-}$ was recovered. PEI induces membrane holes by local removal of the lipid bilayer,[18] so the probe can diffuse through the pore to reach the electrode.

Various types of cationic nanoparticles had previously been observed to induce defects in supported lipid bilayers by hole formation or membrane erosion.[10,18] To demonstrate this effect by electrochemistry, we prepared cationic cysteamine-capped QDs (CA-QDs) using the identical CdSe/ZnS core/shells as for the DPA-QDs (Supporting Information). We incubated the membrane-modified electrode with 10 nM CA-QDs for 1 h. In contrast to our experiments with DPA-QDs, the probe current recovered slightly with CA-QDs (Supporting Information, Figure S1), indicating that these positively charged QDs caused a defect-induced permeation of the membrane by the $[Fe(CN)_6]^{3-}$ probe.

Surface-Enhanced Infrared Absorption Spectroscopy (SEIRAS) of DPA-QDs on Planar Membranes. In near-field distance to a nanostructured metal film, the infrared absorption of molecules is enhanced by a factor of 10−1000.[37] Taking advantage of this phenomenon, SEIRAS allows molecular information to be detected from single monolayers, for example, for *in situ* investigations of the assembly of the molecules at interfaces. SEIRAS is an exquisitely sensitive technique which can detect even minute absorption changes (as small as 10^{-5}) such as those induced by protein adsorption to a lipid membrane.[38,39] Here we have employed SEIRAS to study structural changes of model membranes induced by the interaction of DPA-QDs. Importantly, we have chosen the lipid composition so as to mimic RBC membranes. Formation of the planar membrane by vesicle fusion on a preadsorbed DT monolayer on the gold surface was monitored *in situ* by SEIRAS. The spectrum of DT adsorbed onto the gold surface is

shown in Figure 7a (black), taking the bare Au surface immersed in ethanol as the reference spectrum. The abscissa is divided into two wavenumber regions of particular interest, namely, the CH and OH stretching region at ~3000 cm^{-1} and the fingerprint region from 1800 to 1500 cm^{-1}. The left panel of Figure 7a shows bands at 2925 and 2853 cm^{-1} that are assigned to the asymmetric, $\nu_{as}(CH_2)$, and symmetric, $\nu_s(CH_2)$, stretching vibrations of the alkyl chain CH_2 groups, respectively. The bands at 2973 and 2877 cm^{-1} are attributed to the asymmetric, $\nu_{as}(CH_3)$, and symmetric, $\nu_s(CH_3)$, stretching vibrations. Figure 7a shows the SEIRAS spectrum of the bilayer on the DT surface (Figure 5) produced by fusion of vesicles with the lipid composition of the outer leaflet (upper panel, red), taking a DT monolayer immersed in aqueous solution as the reference. The bands at 2925 and 2853 cm^{-1} are attributed to the asymmetric, $\nu_{as}(CH_2)$, and symmetric, $\nu_s(CH_2)$, stretching vibrations of the CH_2 groups, and the band at 1740 cm^{-1} is due to the C═O stretching vibration of the lipid.[40] The strong negative peak at ~1650 cm^{-1} is associated with the OH bending vibration of water, indicating a highly hydrophobic environment in the lipid bilayer. After formation of the planar bilayer, the spectrum of a membrane-modified Au surface immersed in PBS was taken as the reference, and 10 nM DPA-QDs (in PBS) was added before recording an FTIR spectrum. The DPA-QD-induced SEIRAS difference spectrum is shown in Figure 7a (upper panel, blue). The strong band at ~1650 cm^{-1} is broad and asymmetric, suggesting that it consists of several overlapping bands. By Gaussian curve fitting, it can be decomposed into bands at 1593, 1535, 1675, and 1640 cm^{-1}. On the basis of a comparison with the transmission spectrum of DPA in a KBr pellet (Figure 7b, black), the two peaks at 1593 and 1535 cm^{-1} are assigned to the asymmetric bending modes of $-NH_3^+$, δ_{as} ($-NH_3^+$), of DPA.[41] The bands at 1675 and 1640 cm^{-1} are known to arise from the δ_{as} ($-NH_3^+$) and the asymmetric stretching vibration of the $-COO^-$ group, $\nu_{as}(-COO^-)$, overlapping with a weak water absorption band.[41,42] These characteristic peaks clearly reveal that, when interacting with the lipid bilayer, the DPA ligands on the QDs are in their zwitterionic form. Interestingly, bands attributed to the asymmetric $\nu_{as}(CH_2)$ and symmetric $\nu_s(CH_2)$ stretching vibrations of the CH_2 groups appear upon addition of DPA-QDs (Figure 7a, left). These are also shown enlarged in the inset of Figure 7a (blue). These peaks were not observed in the transmission spectrum of DPA in a KBr pellet (Figure 7b, black), however. Consequently, they signal a change of the lipid structure induced by the interaction of DPA-QDs with the planar membranes. Compared with the $\nu_{as}(CH_2)$ and $\nu_s(CH_2)$ stretching vibrations of the lipid bilayer (Figure 7a, inset) at 2925 and 2853 cm^{-1}, the $\nu_{as}(CH_2)$ and $\nu_s(CH_2)$ peaks induced by adding DPA-QDs are slightly blue-shifted to 2929 and 2857 cm^{-1}, respectively. Since the $\nu_{as}(CH_2)$ and $\nu_s(CH_2)$ vibrations are sensitive to the conformation of alkyl chains, their peak shifts have often been utilized to monitor structure and phase changes in phospholipid systems.[43,44] The blue shifts of the CH_2 stretching bands upon DPA-QD−membrane interaction observed here indicate a more fluid and flexible conformation.[45] In agreement with this result, it was recently reported that negatively charged quantum dots softened a zwitterionic lipid bilayer.[13]

Likewise, we have studied DPA-QD interacting with lipid membranes having the lipid composition of the inner bilayer leaflet of RBC plasma membranes. SEIRAS data from samples prepared by vesicle fusion on the DT/Au surface are also shown in Figure 7a (lower panel, red). Compared with the spectrum of the outer lipid layer (upper panel, red), the bands assigned to $\nu_{as}(CH_2)$ and $\nu_s(CH_2)$ are broader because of overlap with $\nu_{as}(CH_3)$ and $\nu_s(CH_3)$, respectively. The C═O stretching band at 1731 cm^{-1} is also visible, but we did not observe the negative band at ~1650 cm^{-1}. These differences indicate a more disordered bilayer conformation and a less hydrophobic inner microenvironment. In the SEIRAS difference spectrum in the presence of DPA-QDs (Figure 7a, lower panel, blue), a broad band appears at ~1640 cm^{-1}, as was also the case for the model membrane with the lipid composition of the RBC outer lipid leaflet. Gaussian curve fitting shows bands at 1593, 1645, and 1675 cm^{-1} assigned to the vibration of the zwitterionic DPA ligand. An additional peak at 1742 cm^{-1}, assigned to the stretching vibration of C═O, likely results from a hydrogen bond formed between the $-COO^-$ group of the DPA ligands on the nanoparticles and a positive group on the surface of the lipid. This interaction might facilitate the movement of the DPA-QDs to the inner leaflet of the lipid bilayer. After adding DPA-QDs, we again observed the bands attributed to $\nu_{as}(CH_2)$ and $\nu_s(CH_2)$, indicating that interactions of DPA-QDs with the inner lipid leaflet of RBC membranes enhance the structural flexibility of the bilayer. As a conclusion, DPA-QDs interacting with either side of the lipid bilayer of the RBC membranes soften the lipid structure, which might facilitate the penetration of DPA-QDs into the lipid bilayer without pore formation.

Recently, evidence was shown that hole formation in a membrane induced by penetrating nanoparticles can be avoided by modulating nanoparticle surface charge density or structure.[11,23] Cationic Au nanoparticles with 50% charge density relative to hydrophobic ligands were found to effectively penetrate the lipid membrane without forming holes, whereas significant membrane disruption was observed at higher charge densities. Membrane penetration without pore formation was also seen in MD simulations of the translocation of peptides containing charged amino acids.[46] Certain cell-penetrating peptides are also known to

cross membranes without lipid bilayer disruption.[47−49] As a conclusion, while a positive net charge ensures the penetrating property of nanoparticles, a high charge density promotes membrane disruption. Our DPA-QDs are coated with a small, zwitterionic amino acid ligand for which the charges on the amino and carboxylic acid groups are balanced, enabling them to penetrate lipid membranes without affecting the bilayer integrity.

CONCLUSIONS

Mechanisms of membrane penetration by synthetic nanoparticles are currently under intense investigation. By combining confocal fluorescence microscopy, electrochemistry, and SEIRAS, we have studied interactions between small DPA-QDs of 4 nm radius and lipid membranes, including the RBC plasma membrane and planar model lipid layers on solid supports having identical lipid compositions as the RBC inner and outer membrane layers. Confocal microscopy showed that incubation of RBCs with 10 nM DPA-QDs resulted in membrane penetration and intracellular internalization with a half-life of 1.7 h. Interaction of DPA-QDs with RBCs did not cause membrane deformation on the resolution scale of optical microscopy. On the molecular level, however, SEIRAS experiments revealed that the interactions of DPA-QDs with model lipid bilayers led to a softening of the lipid and resulted in a more flexible conformation. The electrochemistry studies yielded clear evidence that penetration of DPA-QDs into the lipid membranes did not lead to the formation of (ion-conducting) pores. We believe that the zwitterionic nature of the ligands on our QDs is responsible for the observed membrane penetration without pore formation. To conclude, we have shown that nanoparticles can be functionalized with appropriate ligands to render them membrane-permeant while avoiding severe cytotoxicity associated with the formation of pores in the plasma membrane.

METHODS

Nanoparticle Preparation and Characterization. DPA-QDs were prepared as reported previously.[28] Briefly, CdSe/ZnS core/shell QDs were synthesized in organic solvent prior to ligand exchange with DPA, yielding water-soluble zwitterionic nanoparticles. The fluorescence emission spectrum of the DPA-QDs showed a peak at 591 nm (SPEX Fluorolog II, Horiba Jobin Yvon, Edison, NJ); a hydrodynamic radius of 4.0 ± 0.3 nm was determined by fluorescence correlation spectroscopy using a home-built confocal microscope.[50,51]

Red Blood Cells (RBCs). Human blood samples were freshly collected from multiple healthy adult volunteers in the Hospital of Changchun University of Chinese Medicine. Whole blood was centrifuged at 2000 rpm for 3 min, and plasma, buffy coat, and top layer of cells were decanted. The remaining packed RBCs were washed three times with sterile phosphate buffered saline (PBS).

Live Cell Confocal Imaging. After washing, 25 μL of packed RBCs was dissolved in 10 mL of PBS. The diluted RBC suspension (200 μL) was cultured for 20 min at 37 °C and 5% CO_2 in 8-well LabTek chambers (Nunc, Langenselbold, Germany) that were coated by exposure to 0.1 mg/mL poly-L-lysin for 10 min. Afterward, the cells were rinsed three times with PBS. For nanoparticle exposure, cells were incubated with 200 μL of 10 nM DPA-QDs in PBS by solution exchange (unless stated otherwise). The cells were imaged after 1 and 4 h by using a spinning disk confocal laser microscope assembled from individual components.[7,52] Briefly, it consists of an inverted microscope body (Axio Observer, Zeiss, Göttingen, Germany), a CSU 10 spinning disk unit (Yokogawa Electric, Tokyo, Japan), four solid-state lasers (405, 473, 532, and 637 nm) for excitation, an image splitter unit, and an EMCCD camera (DV-887, Andor, Belfast, UK).[28] Nanoparticles were excited at 532 nm; the emission was collected through a band-pass filter (HQ 585/80, AHF, Tübingen, Germany). For quenching experiments, cells were rinsed three times with 200 μL of PBS and incubated with 200 μL of QSY 9 succinimidyl ester (Invitrogen) at a concentration of 5 μg/mL. After 10 min, the cells were washed three times with 200 μL of PBS. For 3D reconstruction, after quenching with QSY 9, the plasma membrane was stained with CellMask deep red (Invitrogen) at 0.25 μg/mL in PBS solution for 5 min, then washed three times with PBS. The red membrane dye was excited at 637 nm, and the emission was filtered through a long-pass filter (FF01-635/LP, AHF). Z-stacks were recorded at 0.2 μm spacing in two separate spectral channels. Processing and visualization of 3D images was performed by the image processing software IMARIS (Bitplane, Zurich, Switzerland).

Alternatively, after cell washing, 25 μL of packed RBCs was diluted to 500 μL with PBS. Then, 10 μL of RBCs was taken from the 500 μL stock solution and diluted to 200 μL with DPA-QDs at a concentration of 10 nM in PBS. Aliquots prepared in this way were kept in a humidified incubator at 37 °C and 5% CO_2 for 1 h (or 2, 4, 8 h), and then centrifuged at 2000 rpm for 3 min. The sedimented cells were introduced into the channel of a sandwich sample cell (Ibidi, Germany). After waiting for 20 min for the cells to adhere to the surface of the bottom glass slide, the channel was rinsed with fresh portions of buffer to remove nonadhering cells. The cells were imaged using a confocal laser scanning fluorescence microscope (CLSM, Leica TCS SP2, Leica Microsystems, Mannheim, Germany). Nanoparticles were excited at 488 nm and observed through a 550−650 nm emission band-pass filter.

For tracer dye leaking experiment, 10 μL of RBCs was incubated with calcein violet AM (Invitrogen) at a concentration of 10 μM in PBS for 60 min at 37 °C and 5% CO_2. Then, the RBCs were centrifuged, washed three times with PBS, and exposed to 10 nM DPA-QDs for 6 h in a humidified incubator at 37 °C and 5% CO_2. Afterward, the cells were introduced into the channel of the sandwich sample cell and imaged by CLSM. The tracer dye was excited at 405 nm and observed through a 450−530 nm emission band-pass. Nanoparticles were excited at 488 nm and observed through a 550−650 nm emission band-pass .

Electrochemical Measurements. Cyclic voltammograms were recorded with a Mode 630 electrochemical analyzer (CH Instruments, Austin, TX). All experiments were carried out with a three-electrode system consisting of an Ag/AgCl (saturated KCl) reference electrode, platinum coils as an auxiliary electrode, and a gold electrode as a working electrode (A = 0.0113 cm^2).

***In Situ* Surface-Enhanced IR Absorption Spectroscopy (SEIRAS).** The experimental setup and procedures for SEIRAS have been described elsewhere.[53] Briefly, a thin gold film was formed on the flat surface of a triangular silicon prism by chemical deposition. The surface of the Si substrate was polished with aluminum oxide powder of 1 μm in size, followed by immersion in a 40 wt % aqueous solution of NH_4F for 1 min. Subsequently, the flat surface of the Si prism was exposed to a 1:1:1 volume mixture of (1) 0.03 M $NaAuCl_4$, (2) 0.3 M Na_2SO_4 + 0.1 M $Na_2S_2O_3$ + 0.1 M

NH_4Cl, and (3) 2.5 vol % HF solution for 90 s to get a shiny Au film. Because the Au surface may still be contaminated with chemicals, these were removed by electrochemical cycling of the potential between 0.1 and 1.4 V in 0.1 mol L^{-1} H_2SO_4 until the cyclic voltammogram of polycrystalline gold appeared. After electrochemical cleaning, the gold-coated prism was mounted into a polytrifluorochloroethylene cell. The IR beam of the FTIR spectrometer (IFS 66s/v, Bruker, Ettlingen, Germany) was coupled into the silicon prism at an incident angle of 60°, and the reflected beam intensity was recorded with a liquid-nitrogen-cooled MCT detector.

Preparation of Supported Lipid Bilayer Membranes. Egg PC, SM, and cholesterol (Sigma-Aldrich, St. Louis, MO) were mixed in ratios of 1:1:1 (by weight); DOPE, DOPS, and cholesterol (Sigma-Aldrich) were mixed in ratios of 2:1:1 (by weight). The mixtures were suspended in chloroform, and the solvent was removed in a N_2 stream to initiate the formation of a thin lipid layer, followed by treatment in a vacuum chamber for 30 min. Double distilled water was added to yield a final concentration of 1 mg/mL. Sonication (Kunsan Instrument, Jiangsu, China) at 40 °C for 1 h yielded a clear solution. The vesicles were always used within 24 h after preparation. A freshly prepared gold electrode was immersed into 1 mM 1-dodecanethiol (DT, Sigma-Aldrich) dissolved in ethanol for 20 min. After thorough rinsing with ethanol and water, the electrode was immersed into the vesicle solution for 2−4 h to enable formation of the planar membrane on the surface by vesicle fusion. The interaction between the DPA-QDs and the planar membrane was initiated by soaking a lipid/DT/Au electrode in a solution of 10 nM DPA-QDs. After application of nanoparticles, the electrode was immersed in a 1% poly(ethyleneimine) (PEI, Sigma-Aldrich) solution for 1 h.

Acknowledgment. This work was supported by the Youth Foundation of China (21105097), President Funds of the Chinese Academy of Sciences, Youth Foundation of Jilin Province (201101081), and the Deutsche Forschungsgemeinschaft (DFG) through the Center for Functional Nanostructures (CFN) and Schwerpunktprogramm (SPP) 1313, Grants NI 291/7 and NI 291/8. We gratefully acknowledge support by Professor Erkang Wang, Professor Shaojun Dong, and Dr. Carlheinz Röcker.

Supporting Information Available: Additional experimental details and figures. This material is available free of charge *via* the Internet at http://pubs.acs.org.

REFERENCES AND NOTES

1. Grobe, A.; Renn, O.; Jaeger, A. Risk Governance of Nanotechnology Applications in Food and Cosmetics; available from http://www.irgc.org/IMG/pdf/IRGC_Report_FINAL_For_Web.pdf (accessed Feb. 26, 2010).
2. Liu, J.; Lau, S. K.; Varma, V. A.; Kairdolf, B. A.; Nie, S. Multiplexed Detection and Characterization of Rare Tumor Cells in Hodgkin's Lymphoma with Multicolor Quantum Dots. *Anal. Chem.* **2010**, *82*, 6237–6243.
3. Maesaki, S. Drug Delivery System of Anti-fungal and Parasitic Agents. *Curr. Pharm. Des.* **2002**, *8*, 433–440.
4. Lewin, M.; Carlesso, N.; Tung, C.-H.; Tang, X.-W.; Cory, D.; Scadden, D. T.; Weissleder, R. Tat Peptide-Derivatized Magnetic Nanoparticles Allow *In Vivo* Tracking and Recovery of Progenitor Cells. *Nat. Biotechnol.* **2000**, *18*, 410–414.
5. Colvin, V. L. The Potential Environmental Impact of Engineered Nanomaterials. *Nat. Biotechnol.* **2003**, *21*, 1166–1170.
6. Nel, A. E.; Mädler, L.; Velegol, D.; Xia, T.; Hoek, E. M. V.; Somasundaran, P.; Klaessig, F.; Castranova, V.; Thompson, M. Understanding Biophysicochemical Interactions at the Nano-Bio Interface. *Nat. Mater.* **2009**, *8*, 543–557.
7. Jiang, X.; Dausend, J.; Hafner, M.; Musyanovych, A.; Röcker, C.; Landfester, K.; Mailänder, V.; Nienhaus, G. U. Specific Effects of Surface Amines on Polystyrene Nanoparticles in Their Interactions with Mesenchymal Stem Cells. *Biomacromolecules* **2010**, *11*, 748–753.
8. Jiang, X.; Weise, S.; Hafner, M.; Röcker, C.; Zhang, F.; Parak, W. J.; Nienhaus, G. U. Quantitative Analysis of the Protein Corona on FePt Nanoparticles Formed by Transferrin Binding. *J. Roy. Soc. Interface* **2010**, *7*, S5–S13.
9. Verma, A.; Stellacci, F. Effect of Surface Properties on Nanoparticle−Cell Interactions. *Small* **2010**, *6*, 12–21.
10. Lovrić, J.; Bazzi, H. S.; Cuie, Y.; Fortin, G. R. A.; Winnik, F. M.; Maysinger, D. Differences in Subcellular Distribution and Toxicity of Green and Red Emitting CdTe Quantum Dots. *J. Mol. Med.* **2005**, *83*, 377–385.
11. Verma, A.; Uzun, O.; Hu, Y.; Hu, Y.; Han, H.-S.; Watson, N.; Chen, S.; Irvine, D. J.; Stellacci, F. Surface-Structure-Regulated Cell-Membrane Penetration by Monolayer-Protected Nanoparticles. *Nat. Mater.* **2008**, *7*, 588–595.
12. Choleris, E.; Little, S. R.; Mong, J. A.; Puram, S. V.; Langer, R.; Pfaff, D. W. Microparticle-Based Delivery of Oxytocin Receptor Antisense DNA in the Medial Amygdala Blocks Social Recognition in Female Mice. *Proc. Natl. Acad. Sci. U.S.A.* **2007**, *104*, 4670–4675.
13. Zhang, X.; Yang, S. Nonspecific Adsorption of Charged Quantum Dots on Supported Zwitterionic Lipid Bilayers: Real-Time Monitoring by Quartz Crystal Microbalance with Dissipation. *Langmuir* **2011**, *27*, 2528–2535.
14. Dif, A. l.; Henry, E.; Artzner, F.; Baudy-Floc'h, M. l.; Schmutz, M.; Dahan, M.; Marchi-Artzner, V. R. Interaction between Water-Soluble Peptidic CdSe/ZnS Nanocrystals and Membranes: Formation of Hybrid Vesicles and Condensed Lamellar Phases. *J. Am. Chem. Soc.* **2008**, *130*, 8289–8296.
15. Laurencin, M.; Georgelin, T.; Malezieux, B.; Siaugue, J.-M.; Ménager, C. Interactions between Giant Unilamellar Vesicles and Charged Core−Shell Magnetic Nanoparticles. *Langmuir* **2010**, *26*, 16025–16030.
16. Leroueil, P. R.; Hong, S.; Mecke, A.; Baker, J. R.; Orr, B. G.; Holl, M. M. B. Nanoparticle Interaction with Biological Membranes: Does Nanotechnology Present a Janus Face? *Acc. Chem. Res.* **2007**, *40*, 335–342.
17. Roiter, Y.; Ornatska, M.; Rammohan, A. R.; Balakrishnan, J.; Heine, D. R.; Minko, S. Interaction of Nanoparticles with Lipid Membrane. *Nano Lett.* **2008**, *8*, 941–944.
18. Leroueil, P. R.; Berry, S. A.; Duthie, K.; Han, G.; Rotello, V. M.; McNerny, D. Q.; Baker, J. R.; Orr, B. G.; Holl, M. M. B. Wide Varieties of Cationic Nanoparticles Induce Defects in Supported Lipid Bilayers. *Nano Lett.* **2008**, *8*, 420–424.
19. Yu, J.; Patel, S. A.; Dickson, R. M. *In Vitro* and Intracellular Production of Peptide-Encapsulated Fluorescent Silver Nanoclusters. *Angew. Chem., Int. Ed.* **2007**, *46*, 2028–2030.
20. Kostarelos, K.; Lacerda, L.; Pastorin, G.; Wu, W.; Wieckowski, S.; Luangsivilay, J.; Godefroy, S.; Pantarotto, D.; Briand, J.-P.; Muller, S.; Prato, M.; Bianco, A. Cellular Uptake of Functionalized Carbon Nanotubes Is Independent of Functional Group and Cell Type. *Nat. Nanotechnol.* **2007**, *2*, 108–113.
21. Cho, E. C.; Xie, J. W.; Wurm, P. A.; Xia, Y. N. Understanding the Role of Surface Charges in Cellular Adsorption *versus* Internalization by Selectively Removing Gold Nanoparticles on the Cell Surface with a I_2/KI Etchant. *Nano Lett.* **2009**, *9*, 1080–1084.
22. Zhao, Y.; Sun, X.; Zhang, G.; Trewyn, B. G.; Slowing, I. I.; Lin, V. S.-Y. Interaction of Mesoporous Silica Nanoparticles with Human Red Blood Cell Membranes: Size and Surface Effects. *ACS Nano* **2011**, *5*, 1366–1375.
23. Lin, J. Q.; Zhang, H. W.; Chen, Z.; Zheng, Y. G. Penetration of Lipid Membranes by Gold Nanoparticles: Insights into Cellular Uptake, Cytotoxicity, and Their Relationship. *ACS Nano* **2010**, *4*, 5421–5429.
24. Michalet, X.; Pinaud, F. F.; Bentolila, L. A.; Tsay, J. M.; Doose, S.; Li, J. J.; Sundaresan, G.; Wu, A. M.; Gambhir, S. S.; Weiss, S. Quantum Dots for Live Cells, *In Vivo* Imaging, and Diagnostics. *Science* **2005**, *307*, 538–544.
25. Chan, W. C. W.; Nie, S. M. Quantum Dot Bioconjugates for Ultrasensitive Nonisotopic Detection. *Science* **1998**, *281*, 2016–2018.
26. Lidke, D. S.; Nagy, P.; Heintzmann, R.; Arndt-Jovin, D. J.; Post, J. N.; Grecco, H. E.; Jares-Erijman, E. A.; Jovin, T. M. Quantum Dot Ligands Provide New Insights into ErbB/HER Receptor-Mediated Signal Transduction. *Nat. Biotechnol.* **2004**, *22*, 198–203.

27. Bruchez, M.; Moronne, M.; Gin, P.; Weiss, S.; Alivisatos, A. P. Semiconductor Nanocrystals as Fluorescent Biological Labels. *Science* **1998**, *281*, 2013–2016.
28. Breus, V. V.; Heyes, C. D.; Tron, K.; Nienhaus, G. U. Zwitterionic Biocompatible Quantum Dots for Wide pH Stability and Weak Nonspecific Binding to Cells. *ACS Nano* **2009**, *3*, 2573–2580.
29. Jiang, X.; Röcker, C.; Hafner, M.; Brandholt, S.; Dörlich, R. M.; Nienhaus, G. U. Endo- and Exocytosis of Zwitterionic Quantum Dot Nanoparticles by Live HeLa Cells. *ACS Nano* **2010**, *4*, 6787–6797.
30. Underhill, D. M.; Ozinsky, A. Phagocytosis of Microbes: Complexity in Action. *Annu. Rev. Immunol.* **2002**, *20*, 825–852.
31. Mühlfeld, C.; Gehr, P.; Rothen-Rutishauser, B. Translocation and Cellular Entering Mechanisms of Nanoparticles in the Respiratory Tract. *Swiss Med. Wkly.* **2008**, *138*, 387–391.
32. Geiser, M.; Rothen-Rutishauser, B.; Kapp, N.; Schürch, S.; Kreyling, W.; Schulz, H.; Semmler, M.; Hof, V. I.; Heyder, J.; Gehr, P. Ultrafine Particles Cross Cellular Membranes by Nonphagocytic Mechanisms in Lungs and in Cultured Cells. *Environ. Health Perspect.* **2005**, *113*, 1555–60.
33. Rothen-Rutishauser, B.; Schürch, S.; Haenni, B.; Kapp, N.; Gehr, P. Interaction of Fine Particles and Nanoparticles with Red Blood Cells Visualized with Advanced Microscopic Techniques. *Environ. Sci. Technol.* **2006**, *40*, 4353–4359.
34. Rejman, J.; Oberle, V.; Zuhorn, I. S.; Hoekstra, D. Size-Dependent Internalization of Particles *via* the Pathways of Clathrin- and Caveolae-Mediated Endocytosis. *Biochem. J.* **2004**, *377*, 159–169.
35. Asharani, P. V.; Sethu, S.; Vadukumpully, S.; Zhong, S.; Lim, C. T.; Hande, M. P.; Valiyaveettil, S. Investigations on the Structural Damage in Human Erythrocytes Exposed to Silver, Gold, and Platinum Nanoparticles. *Adv. Funct. Mater.* **2010**, *20*, 1233–1242.
36. Tanford, C. *The Hydrophobic Effect*; John Wiley & Sons, Inc.: New York, 1980; pp 109−110.
37. Osawa, M. Surface-Enhanced Infrared Absorption. *Top. Appl. Phys.* **2001**, *81*, 163–187.
38. Jiang, X.; Zaitseva, E.; Schmidt, M.; Siebert, F.; Engelhard, M.; Schlesinger, R.; Ataka, K.; Vogel, R.; Heberle, J. Resolving Voltage-Dependent Structural Changes of a Membrane Photoreceptor by Surface-Enhanced IR Difference Spectroscopy. *Proc. Natl. Acad. Sci. U.S.A.* **2008**, *105*, 12113–12117.
39. Jiang, X.; Engelhard, M.; Ataka, K.; Heberle, J. Molecular Impact of the Membrane Potential on the Regulatory Mechanism of Proton Transfer in Sensory Rhodopsin II. *J. Am. Chem. Soc.* **2010**, *132*, 10808–10815.
40. Ataka, K.; Giess, F.; Knoll, W.; Naumann, R.; Haber-Pohlmeier, S.; Richter, B.; Heberle, J. Oriented Attachment and Membrane Reconstitution of His-Tagged Cytochrome *c* Oxidase to a Gold Electrode: *In Situ* Monitoring by Surface-Enhanced Infrared Absorption Spectroscopy. *J. Am. Chem. Soc.* **2004**, *126*, 16199–16206.
41. Bieri, M.; Bürgi, T. D-Penicillamine Adsorption on Gold: An *In Situ* ATR-IR Spectroscopic and QCM Study. *Langmuir* **2006**, *22*, 8379–8386.
42. Colthup, N. B.; Daly, L. H.; Wiberley, S. E. *Introduction to Infrared and Raman Spectroscopy*; Academic Press: New York, 1990.
43. Xia, Y.; Venkateswaran, N.; Qin, D.; Tien, J.; Whitesides, G. M. Use of Electroless Silver as the Substrate in Microcontact Printing of Alkanethiols and Its Application in Microfabrication. *Langmuir* **1998**, *14*, 363–371.
44. Moore, D. J.; Wyrwa, M.; Reboulleau, C. P.; Mendelsohn, R. Quantitative IR Studies of Acyl Chain Conformational Order in Fatty Acid Homogeneous Membranes of Live Cells of *Acholeplasma laidlawii* B. *Biochemistry* **1993**, *32*, 6281–6287.
45. Mitchell, M. L.; Dluhy, R. A. *In Situ* FT-IR Investigation of Phospholipid Monolayer Phase Transitions at the Air−Water Interface. *J. Am. Chem. Soc.* **1988**, *110*, 712–718.
46. Johansson, A. C. V.; Lindahl, E. Amino-Acid Solvation Structure in Transmembrane Helices from Molecular Dynamics Simulations. *Biophys. J.* **2006**, *91*, 4450–4463.
47. Herbig, M. E.; Assi, F.; Textor, M.; Merkle, H. P. The Cell Penetrating Peptides pVEC and W2-pVEC Induce Transformation of Gel Phase Domains in Phospholipid Bilayers without Affecting Their Integrity. *Biochemistry* **2006**, *45*, 3598–3609.
48. Thorén, P. E. G.; Persson, D.; Isakson, P.; Goksör, M.; Önfelt, A.; Nordén, B. Uptake of Analogs of Penetratin, Tat(48−60) and Oligoarginine in Live Cells. *Biochem. Biophys. Res. Commun.* **2003**, *307*, 100–107.
49. Patel, L. N.; Zaro, J. L.; Shen, W.-C. Cell Penetrating Peptides: Intracellular Pathways and Pharmaceutical Perspectives. *Pharm. Res.* **2007**, *24*, 1977–1992.
50. Schenk, A.; Ivanchenko, S.; Röcker, C.; Wiedenmann, J.; Nienhaus, G. U. Photodynamics of Red Fluorescent Proteins Studied by Fluorescence Correlation Spectroscopy. *Biophys. J.* **2004**, *86*, 384–394.
51. Röcker, C.; Pötzl, M.; Zhang, F.; Parak, W. J.; Nienhaus, G. U. A Quantitative Fluorescence Study of Protein Monolayer Formation on Colloidal Nanoparticles. *Nat. Nanotechnol.* **2009**, *4*, 577–580.
52. Jiang, X.; Musyanovych, A.; Röcker, C.; Landfester, K.; Mailänder, V.; Nienhaus, G. U. Specific Effects of Surface Carboxyl Groups on Anionic Polystyrene Particles in Their Interactions with Mesenchymal Stem Cells. *Nanoscale* **2011**, *3*, 2028–2035.
53. Ataka, K.; Heberle, J. Functional Vibrational Spectroscopy of a Cytochrome *c* Monolayer: SEIDAS Probes the Interaction with Different Surface-Modified Electrodes. *J. Am. Chem. Soc.* **2004**, *126*, 9445–9457.